Conformal coating of ultrathin metal-organic framework on semiconductor electrode for boosted photoelectrochemical water oxidation

Yu-Jie Dong, Jin-Feng Liao, Zi-Cheng Kong, Yang-Fan Xu, Ze-Jie Chen, Hong-Yan Chen*, Dai-Bin Kuang, Dieter Fenske, Cheng-Yong Su*

MOE Key Laboratory of Bioinorganic and Synthetic Chemistry, Lehn Institute of Functional Materials, School of Chemistry, Sun Yat-sen University, Guangzhou 510275, PR China

ARTICLE INFO

ABSTRACT

Exploring efficient photocatalysts for water oxidation is highly demanded because of their significant role in artificial photosynthesis. The research of metal-organic frameworks (MOFs) based photoelectrochemical (PEC) water splitting is promising but still in its infancy due to the challenge to fabricate high-quality MOFs photoelectrode. Here an Fe_2O_3/Fe-based MOF core/shell nanorod is prepared for efficient PEC water oxidation *via* a facile surfactant-assisted solvothermal method. With polyvinylpyrrolidone (PVP) molecules as intermedia, an ultrathin MOF shell of several nanometers thick can be controllably grown on the surface of Fe_2O_3 nanorod. Charge dynamical behaviors study by ultrafast transient absorption spectroscopy (TAS) and photoelectrochemical impedance spectroscopy (PEIS), reveal that the ultrathin MOF shell is crucial to promote the charge separation by providing a cascade band level, but also accelerate the hole injection efficiency *via* exposing more accessible Fe-oxo cluster active sites. Accompanied with good visible-light response, the Ti-doped Fe_2O_3/NH_2-MIL-101(Fe) photoanode delivers a boosted photocurrent density of 2.27 mA cm^{-2} at 1.23 V *vs.* RHE, which is about 2.3 folds of that of pristine Fe_2O_3. This study provides new insights into the rational design of semiconductor/MOFs hybrid materials for photo/photoelectrochemical catalysis.

1. Introduction

Owing to the ever-increasing shortage of energy supply and worsening environmental pollution, artificial photosynthesis has attracted extensive research interest, since it provides a promising pathway to convert the sustainable solar energy into clean H_2 fuels and high-value-added chemicals [1,2]. Exploring efficient photocatalysts for water oxidation is a prerequisite for water splitting because this half reaction involves transfer of four protons and four electrons, which requires stronger driving force and is considered as the most bottleneck step [3,4]. In the context of the search of efficient photocatalysts, metal-organic frameworks (MOFs), constructed by using metal ions or metal-oxo clusters as nodes and organic ligands as linkers, show prospective potential by virtue of the specific crystalline structure featuring in porosity and functionality designability [5,6]. Although impressive advances have realized over the recent years in MOFs photocatalysts for hydrogen generation, few studies were carried out for MOFs towards water oxidation [7–10], probably restricted by the low charge carrier mobility as well as poor stability of most MOFs under water oxidation conditions [11].

In fact, as a promising candidate for photocatalysts, the performance of MOF-based photocatalysts is severely limited by their poor charge separation efficiency due to the poor charge mobility. Although the electron transfer can proceed from organic ligand "antennas" to metal nodes under illumination, the photoinduced carrier is usually inclined to be depleted by the subsequent severe charge recombination before participating in the catalytic reaction restricted by the poor conductivity of organic ligands. Therefore, improving the photo-generated charge separation in MOFs is of supreme importance to boost the catalytic performances. To address this challenge, a possible strategy is to prepare macro/mesoporous or nano-sized MOF particles [12,13], which could make the interior pores accessible by catalytic substrates and reduce the transport distance of charge carriers [14]. In addition, fabricating heterostructure catalyst by coupling MOFs with functional inorganic materials such as noble metal nanoparticle, inorganic semiconductor, *etc.*, also appears to be an attractive solution [15–17]. One commonality of these works is that building an appropriate energy band structure and integrating a synergic action of foreign components are key parameters which have led to improved photocatalytic performance [18,19].

---

* Corresponding authors.
E-mail addresses: chenhy33@mail.sysu.edu.cn (H.-Y. Chen), cesscy@mail.sysu.edu.cn (C.-Y. Su).

Photoelectrochemical (PEC) method offers another effective strategy to enhance the charge separation efficiency of photocatalysts by applying external potential to accelerate the photo-generated carrier separation. However, the development of MOF-based PEC catalysis is largely impeded by the difficulty in fabricating high-quality MOFs photoelectrode. Limited by the poor conductivity, an ideal MOF-based photoelectrode should be rather thin and tightly bonded with the conductive substrate. Coating MOF films onto the surface of nanostructured inorganic semiconductor to form composite electrodes is proposed as a feasible way. Although some MOF films on silicon substrate or semiconductor have been reported by liquid phase epitaxy growth [20,21], electrochemically and dip-coating method [22], these strategies are only suitable for the MOFs that can be synthesized under moderate conditions, *e.g.*, zeolitic imidazolate frameworks (ZIFs) [23,24]. Recently, Liu et al. reported a NH_2-MIL-125 sensitized TiO_2 electrode for PEC water oxidation, and a superior photocurrent density to the pristine TiO_2 photoanode was obtained. However, the water oxidation performance and the film quality are still unsatisfactory [10]. Therefore, the elaborate control of MOF coatings is believed critical to achieve high photoelectric performance [25].

Herein, we develop a facile surfactant-assisted strategy to construct a semiconductor/MOF core/shell heterostructure for efficient PEC water oxidation. To prove this concept, Ti-doped Fe_2O_3 (Fe_2O_3:Ti)/MIL-101(Fe) composite photoanode is fabricated for the first time. Fe-based MOFs are selected because they are environmentally friendly, cost effective, and most importantly, have good visible-light response originated in both the Fe-O cluster and the organic linkers [26,27]. With polyvinylpyrrolidone (PVP) molecules as intermedia, an ultrathin MOF shell of several nanometers thick can be controllably grown on the surface of Fe_2O_3 nanorod. A tight connection was formed between nanoscale uniform MOF shell and Fe_2O_3:Ti core, which enable it to produce efficacy by synergic action of MOFs and hematite, which ultimately lead to excellent PEC performance owing to the promoted light harvesting capability and enhanced charge separation as well as injection efficiency. The oxygen evolution activity of Fe_2O_3:Ti/NH_2-MIL-101(Fe) photoanode outperforms the pristine Fe_2O_3:Ti and other MOF-based photoelectrodes.

2. Experimental section

2.1. Preparation of Fe_2O_3:Ti nanorod array

The titanium doped Fe_2O_3 nanorod (Fe_2O_3:Ti) array was synthesized following a similar hydrothermal procedure as reported previously [28]. In a typical experiment, 1 mmol $FeCl_3 \cdot 6H_2O$ and 1 mmol Na_2SO_4 were dissolved in 20 mL deionized water and transferred to an autoclave. Then, 0.5 mL of 100 mM $TiCl_4$ solution was added dropwisely into the above transparent solution under stirring to obtain a 5% titanium dopant concentration (Ti:Fe = 0.05:1, atomic ratio). Afterwards, FTO glass substrate was placed in the autoclave with the conducting side facing down. Then the hydrothermal reaction was held at 120 ℃ for 4 h in an oven. Thereafter, the as-prepared sample was washed with water and ethanol for several times and dried at 70 ℃. Finally, the sample was annealed in air at 600 ℃ for 1 h to obtain the Fe_2O_3:Ti nanorod array.

2.2. Preparation of Fe_2O_3:Ti/MIL-101(Fe) (Fe_2O_3:Ti/NH_2-MIL-101(Fe)) nanorod composite

The Fe_2O_3:Ti/MOF composite was synthesized through a facile solvothermal process. Briefly, $FeCl_3 \cdot 6H_2O$ and terephthalic (H_2BDC) or 2-aminoterephthalic acid (H_2ATA) were dissolved in DMF solvent with the molar ratio of 2:1 firstly. The mixture was transferred into an autoclave. The as-prepared Fe_2O_3:Ti nanorod film was modified with polyvinylpyrrolidone (PVP, $M_W \approx 24,000$) by immersing it in the DMF solution of PVP for 3 h. Afterwards, both the modified Fe_2O_3:Ti nanorod

film and PVP solution were added into the above autoclave with the nanorod side facing down. The solvothermal reaction was held at 110 ℃ for 20 h in an oven. After cooling down, the film was taken out and rinsed with DMF and ethanol for several times, and finally dried overnight at 70 ℃ in a vacuum oven. Thus, the Fe_2O_3:Ti/MIL-101(Fe) (Fe_2O_3:Ti/NH_2-MIL-101(Fe)) sample was obtained.

2.3. Characterization

The crystalline structure and phase purity of the nanocomposite were determined by X-ray diffraction (XRD, Rigaku Smartlab) using Cu Kα radiation at 40 KV and 30 mA. The nanostructure and morphology were characterized by field emission scanning electron microscopy (FE-SEM, Hitachi SU8010), high-resolution transmission electron microscopy (HRTEM, JEOL-2010 HR). The optical absorption behavior of the samples was studied by the UV–vis spectrometer (Shimadzu UV-3600). X-ray photoelectron spectra (XPS) were investigated on a photoelectron spectrometer (ESCALAB 250, Thermo Fisher Scientific).

Transient absorption spectroscopy from the femtosecond to nanosecond timescale was detected by Helios (Ultrafast Systems LLC) spectrometers equipped with a regeneratively amplified Ti: sapphire laser source (Coherent Legend, 800 nm, 150 fs, 5 mJ pulse^{-1}, and 1 kHz repetition rate) in a transmission mode. Portion of the 710 nm output (75%) pulse was frequency-doubled in a BaB_2O_4 (BBO) crystal, which could generate 355 nm pump light, meanwhile the remaining portion of the output was concentrated into a sapphire window to produce white light continuum (420 nm–780 nm) probe light. The excitation power density is 200 μJ cm^{-2} with the lase repetition rates of 1000 Hz, then transient absorption changes were measured in the visible region from 420 to 780 nm.

2.4. Photoelectrochemical study

The photoelectrochemical (PEC) characterizations of the Fe_2O_3:Ti/MOF composite film were performed in a three-electrode system under AM 1.5 G simulated sunlight of 100 mW cm^{-2} (150 W, Newport 94011 A LCS-100). The as-prepared photoanodes, Pt foil, and Ag/AgCl (in 3 M KCl) electrode were employed as the working, counter, and reference electrode, respectively. All the applied potentials *vs.* Ag/AgCl were converted to values relative to the reversible hydrogen electrode (RHE) according to the equation: $E_{RHE} = E_{Ag/AgCl} + 0.0591 \text{ pH} + E°_{Ag/AgCl}$, where $E_{Ag/AgCl}$ is the measured potential against the reference electrode and $E°_{Ag/AgCl}$ is the standard potential of Ag/AgCl (0.1976 V *vs.* RHE at 25 ℃). An aqueous solution of 1 M NaOH (pH = 13.5) was used as the electrolyte. The electrolyte was purged with N_2 gas for 30 min before the tests. The charge separation efficiency was performed under the same condition except adding H_2O_2 as hole scavenger. The electrolyte was 1 M NaOH or 1 M NaOH with 0.5 M H_2O_2 aqueous solution. The η_{sep} and η_{inj} at a certain applied potential can be obtained by simple calculations: $\eta_{inj} = J_{photo}(H_2O)/J_{photo}(H_2O_2)$; $\eta_{sep} = J_{photo}(H_2O_2)/J_{max}$.

The incident photon-to-current conversion efficiency (IPCE) tests were performed by the Zahner Zennium C-IMPS system (TLS-03) as the function of wavelength from 365 nm to 700 nm at a bias of 1.23 V *vs.* RHE. The photoelectrochemical impedance spectra (PEIS) were carried out on an electrochemical workstation (Zahner Zennium) by applying a frequency ranging from 10 mHz to 100 kHz, with an AC amplitude of 10 mV and a DC bias of 1.23 V *vs.* RHE under simulated sunlight irradiation (AM 1.5 G, 100 mW cm^{-2}). It should be noted that, all the other PEC characterizations except the PEIS and IPCE were conducted on a CHI660 electrochemical workstation.
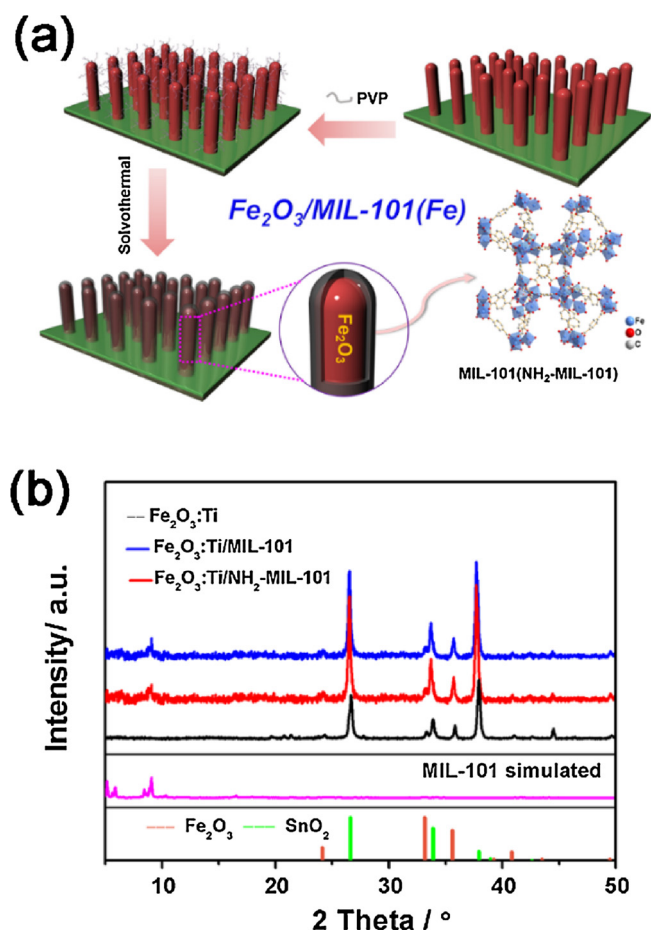
Fig. 1. (a) Schematic of the synthesis process of Fe_2O_3/MIL-101(Fe) core/shell film on FTO substrate *via* surfactant-assisted solvothermal method; (b) XRD patterns of different samples. The green and red line represents the reference SnO_2 (JCPDS No. 41-1445) and hematite (JCPDS No. 33-0664), respectively. (For interpretation of the references to colour in this figure legend, the reader is referred to the web version of this article).

3. Result and discussion

3.1. Preparation of semiconductor/MOFs composite electrode

Due to the composition and structural differences, strategy that bridging semiconductor and MOFs together is quite critical to synthesis tightly contacted heterostructure materials. Here, a simple surfactant-assisted solvothermal method was developed. As illustrated in Fig. 1a, Ti-doped Fe_2O_3 (Fe_2O_3:Ti) nanorod array grown vertically on fluorine-doped tin oxide (FTO) glass substrate was synthesized first with the Ti dopant aiming to improve the conductivity of Fe_2O_3 [29]. Then it was modified with PVP molecules and followed by a solvothermal process to grow MOF shell. As reported previously, PVP is commonly used as surfactant to passivate metal or semiconductor nanoparticle surface through the interaction between metal and the pyrrolidone rings [30]. Therefore, PVP molecule can act as an effective bridging agent in this process for it can be easily adsorbed onto the surface of Fe_2O_3 and then provides nucleation sites for Fe^{3+} adsorption and growth of coordination polymer [31]. Here two Fe-based MOFs of MIL-101 and NH_2-MIL-101 with terephthalic (H_2BDC) or 2-aminoterephthalic acid (H_2ATA) as the organic ligand, respectively, were grown on the

surface of Fe_2O_3:Ti nanorod as model systems. After modified with MIL-101(Fe), the Fe_2O_3:Ti/MIL-101(Fe) showed negligible change in color, while changed from red to dark brown with the NH_2-based one (Fig. S1). Note that Fe_2O_3:Ti/MOF samples shown in the text were

synthesized with PVP concentration of $2\,mg\,mL^{-1}$, except where noted. This surface modification strategy should be quite universal to prepare MOF film on the surface of inorganic semiconductor.

Fig. 1b shows the X-ray powder diffraction (XRD) patterns of as-prepared samples. The pristine Fe_2O_3:Ti nanorod showed typical hematite phase. After decorated with MOFs,

additional diffraction peaks around 10° which agree well with the simulated pattern of MIL-101(Fe) indicated the growth of MOF layer. SEM images (Fig. 2a–c) showed that the Fe_2O_3:Ti nanorods grown on FTO glass had smooth surface with ~750 nm in length, and an average width of 25 nm (the diameter distribution statistics are shown in Fig. S2). After growth of Fe-based MOFs, the length of the nanorods remained the same, while the diameters of the nanorods obviously increased to a range of 30~80 nm for both Fe_2O_3:Ti/MIL-101(Fe) and Fe_2O_3:Ti/NH_2-MIL-101(Fe). Moreover, the interstices of pristine nanorods became smaller and the surface became rougher. Careful comparison revealed that those large nanorods over 60 nm may originate from the coalescent coating of two or three adjacent nanorods by MOF layer. The successful growth of MOF shell was consolidated by TEM images (Fig. 2d and e), which showed the inner single crystalline hematite nanorod had been well covered with a conformal shell of ~5 nm in both Fe_2O_3:Ti/NH_2-MIL-101(Fe) and Fe_2O_3:Ti/ MIL-101(Fe) composite. The X-ray photoelectron spectroscopy (XPS) was further conducted to confirm the formation of MOF shell (Figs. 3, S3 and S4). Compared with pristine Fe_2O_3:Ti, the Fe_2O_3:Ti/NH_2-MIL-101(Fe) showed a distinct N 1s signal as well as enhanced C 1s and O 1s signals. For O 1s spectrum, strong peak at 531.6 eV appeared which can be assigned to C=O in organic ligand, the other two small peaks at 532.5 and 529.9 eV belonged to −OH and Fe−O. For C1s spectrum, four peaks at 284.6, 285.2, 286.4 and 288.5 eV

can be assigned to C=C, C−N, C−C and C=O of ligand, respectively. For N 1s spectrum, two peaks at 399.8 eV and 401.7 eV belonging to N of the $−NH_2$ ($−N=^+$ and $−NH−^+$) were found [32,33]. In addition, Fe 2p spectrum showed two peaks at 711.3 eV and 725.0 eV corresponding to Fe $2p_{2/3}$ and Fe $2p_{1/2}$, respectively, which shifted of 0.7 eV towards high energy compared with that of the as-prepared Fe_2O_3:Ti (710.6 eV and 724.3 eV, respectively). While the values were consistent with the reported Fe(III)-based MOFs [33]. In addition, the characteristic Ti signal ascribed to Fe_2O_3:Ti was not detected in the composite sample. These results, in combine with the C 1s and N 1s spectra, indicated that the surface of Fe_2O_3:Ti was covered completely with the NH_2-MIL-101(Fe) shell. All these results indicated the successfully conformal coating of MOF shell on Fe_2O_3 nanorod.

3.2. Effect of surfactant on the morphology of Fe_2O_3:Ti/MOF nanocomposite

The surface modification with PVP molecules was found to be vital to grow ultrathin MOF shell because it promotes the heterogeneous nucleation and growth of MOF film on the surface of Fe_2O_3:Ti nanorod. In the absence of PVP, only large NH_2-MIL-101 octahedrons ranging from 500 nm to 2 μm were formed on the top of the Fe_2O_3:Ti and showed strong XRD diffraction signals, which should result from the weak affinity between Fe_2O_3:Ti and NH_2-MIL-101 (Figs. S5, S6). This phenomenon was quite similar to that of directly growing NH_2-MIL-101 film on FTO substrate, in the case of which micrometer-sized octahedrons stacked together and tended to detach from the substrate easily. On the contrast, with the assistance of PVP molecules, heterogeneous nucleation of MOF on the surface of Fe_2O_3:Ti nanorods was preferred, and the higher PVP concertation led to the thicker of MOF shell, accompanied with dramatically reduced amount of top octahedrons. This is because higher PVP concentration means more PVP molecules can be adsorbed on the surface, which may provide more nucleation sites for MOF growth. The shell thickness can be tuned from about 1–2 nm for 1 PVP sample (PVP/DMF, 1 mg/mL) to ~10 nm for 5 PVP sample (PVP/DMF, 5 mg/mL). Such uniform NH_2-MIL-101 shell suggested that PVP
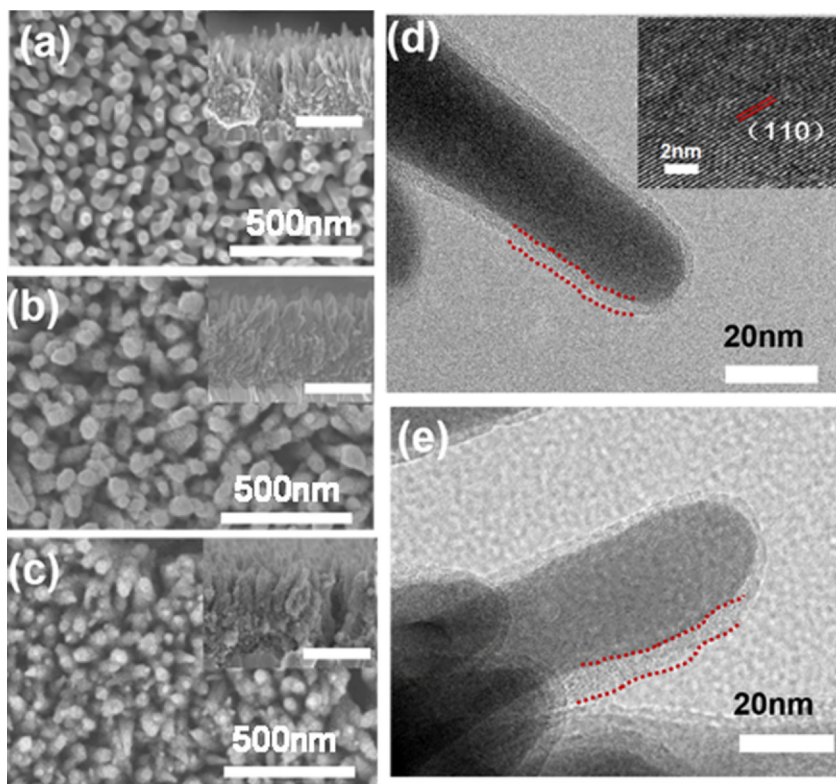
Fig. 2. Top-view and cross-sectional (inset, scale bars: 500 nm) SEM images of Fe_2O_3:Ti nanorod array (a), Fe_2O_3:Ti/MIL-101(Fe) (b) and Fe_2O_3:Ti/NH_2-MIL-101(Fe) (c); TEM images of Fe_2O_3:Ti/MIL-101(Fe) (d) and Fe_2O_3:Ti/NH_2-MIL-101(Fe) (e), respectively. The inset of (d) shows the lattice fringe of the core Fe_2O_3:Ti nanorod and the light-colored part marked with red dotted line shows the MOF shell. (For interpretation of the references to colour in this figure legend, the reader is referred to the web version of this article).
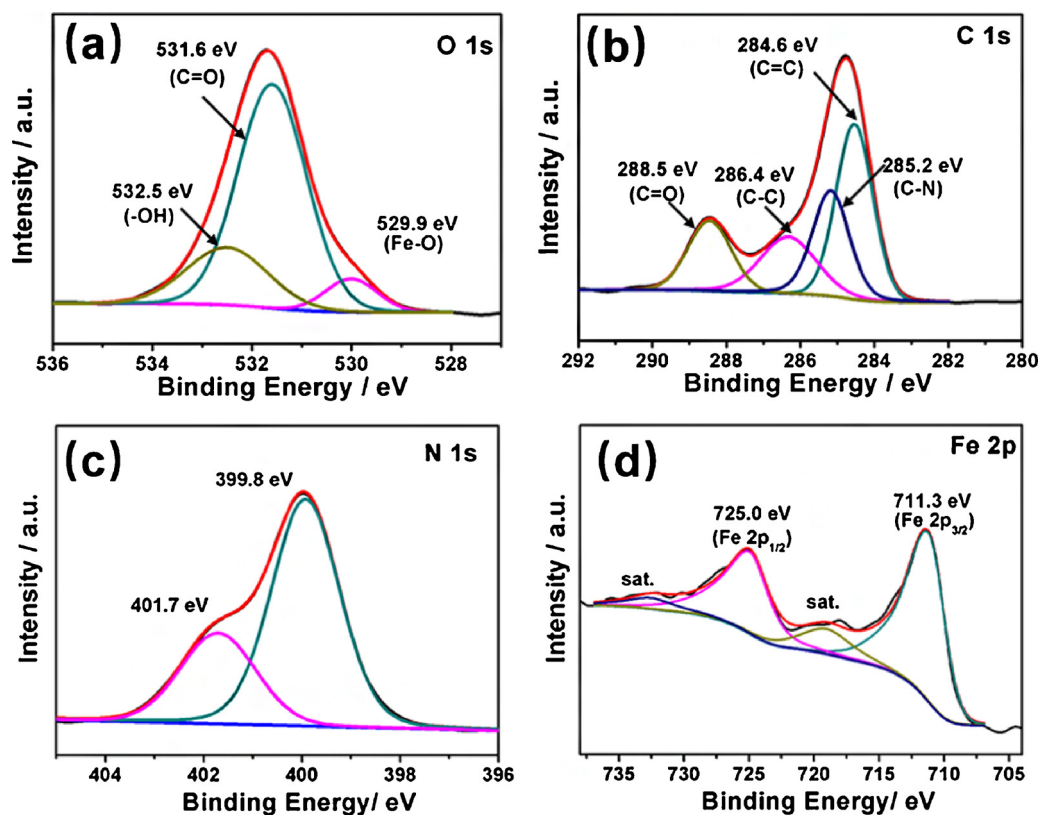
Fig. 3. XPS spectra of Fe_2O_3:Ti/NH_2-MIL-101(Fe) sample: (a) O 1s, (b) C 1s, (c) N 1s, (d) Fe 2p region.

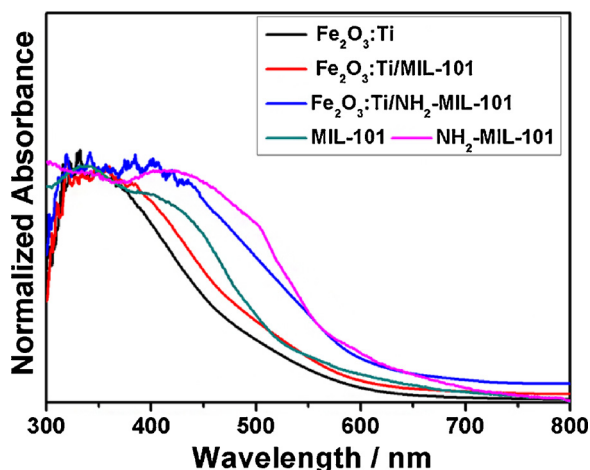**Fig. 4.** UV–vis spectra of Fe$_2$O$_3$:Ti, MIL-101(Fe), NH$_2$-MIL-101(Fe), Fe$_2$O$_3$:Ti/ MIL-101(Fe) and Fe$_2$O$_3$:Ti/NH$_2$-MIL-101(Fe) film. (For interpretation of the references to colour in the text, the reader is referred to the web version of this article).

can offer dispersed nucleation sites for the MOF shell growth. The high-quality MOF coating should be quite beneficial to excellent photo-electrical catalytic performance.

3.3. Optical characterizations of Fe$_2$O$_3$:Ti/MOF nanocomposite

It is known that NH$_2$-MIL-101(Fe) is a special kind of MOF that both the organic ligand and the Fe-O cluster exhibit visible-light responses. Thus decorating Fe$_2$O$_3$:Ti nanorod with NH$_2$-MIL-101(Fe) shell should expand the visible light absorption effectively. For comparison, the light absorption of single MIL-101(Fe) and NH$_2$-MIL-101(Fe) were also measured. As shown in Fig. 4, the pristine Fe$_2$O$_3$:Ti sample showed a strong absorption band in the range of 300–600 nm with an absorption band edge of 590 nm and a band gap of 2.1 eV (Fig. S7), which was in good agreement with the value from literature [34]. After modified

with MOF layer, the Fe$_2$O$_3$:Ti/MIL-101(Fe) sample showed slightly enhanced visible light absorption though the absorption edge did not change obviously. While with the functionalization of amino group, the light absorption of Fe$_2$O$_3$:Ti/NH$_2$-MIL-101(Fe) enhanced largely and the absorption band edge red shifted slightly to ~620 nm with the band gap calculated to be ~1.9 eV. The broadened light absorption was attributed to the contribution of MOF shell. This change in the absorption spectra was also in line with the color change of the films (Fig. S1). Moreover, the absorption behavior was also affected by the morphology of NH$_2$-MIL-101(Fe) shell (Fig. S8). Compared with uniform NH$_2$-MIL-101(Fe) coating films, samples with big octahedron particles on the top of film exhibited stronger absorption due to the large loading amount of MOF. The absorption intensity of MOF film can be increased further by increasing the coating thickness.

3.4. PEC performance for water oxidation

The PEC performances of as-prepared electrodes were examined in a three-electrode configuration with Pt foil and Ag/AgCl electrode as counter and reference electrode, respectively. The 1 M NaOH aqueous solution (pH = 13.5) was used as electrolyte. Fig. 5a shows the linear sweep voltammetry (LSV) plots of different photoelectrodes under AM 1.5 G illumination (100 mW cm^{-2}). All samples showed negligible dark current in the potential range from 0.5 to 1.6 V *vs*. RHE. The pristine Fe$_2$O$_3$:Ti nanorod exhibited an onset potential of 0.92 V and a photocurrent density of 0.98 mA cm^{-2} at 1.23 V *vs*. RHE, similar to those which

synthesized *via* similar method [28]. In comparison, the photocurrent density was improved to 1.26 mA cm^{-2} after modified with MIL-101, and the value can be greatly improved to 2.27 mA cm^{-2} when the MIL-101(Fe) was substituted by NH$_2$-MIL-101(Fe), corresponding to a highest 1.3-fold enhancement. The onset potential showed negligible shift after MOF modification. Meanwhile, the light response test by recording photocurrent density as a function of time under chopped light illumination (Fig. 5b) indicated that all photoanodes exhibit repeated and sensitive responses to the illumination after several light on-off cycles under strong oxidation environment, with the value
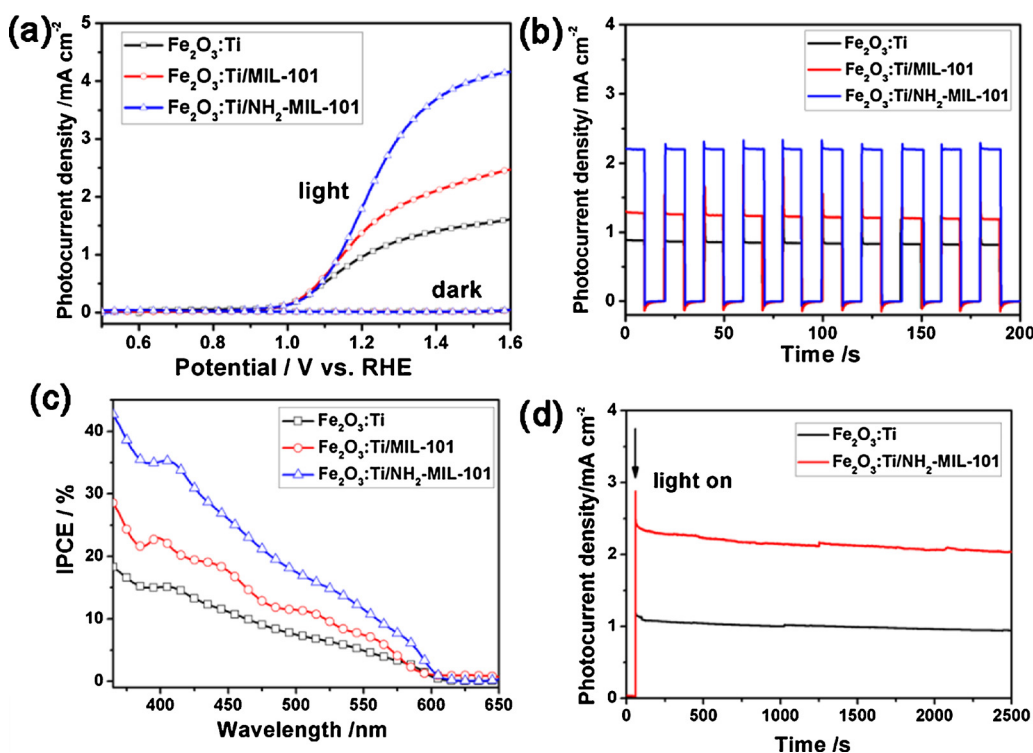

Fig. 5. Photoelectrochemical performance tests of different photoanodes: (a) LSV curves recorded under illumination and dark condition; (b) Amperometric *I-t* curves plotted at 1.23 V *vs*. RHE, under chopped under AM 1.5 G simulated sunlight of 100 mW cm^{-2}; (c) Incident photon-to-current efficiency (IPCE) spectra; (d) Stability tests of Fe$_2$O$_3$:Ti and Fe$_2$O$_3$:Ti/NH$_2$-MIL-101(Fe) photoanode measured at 1.23 V *vs*. RHE.
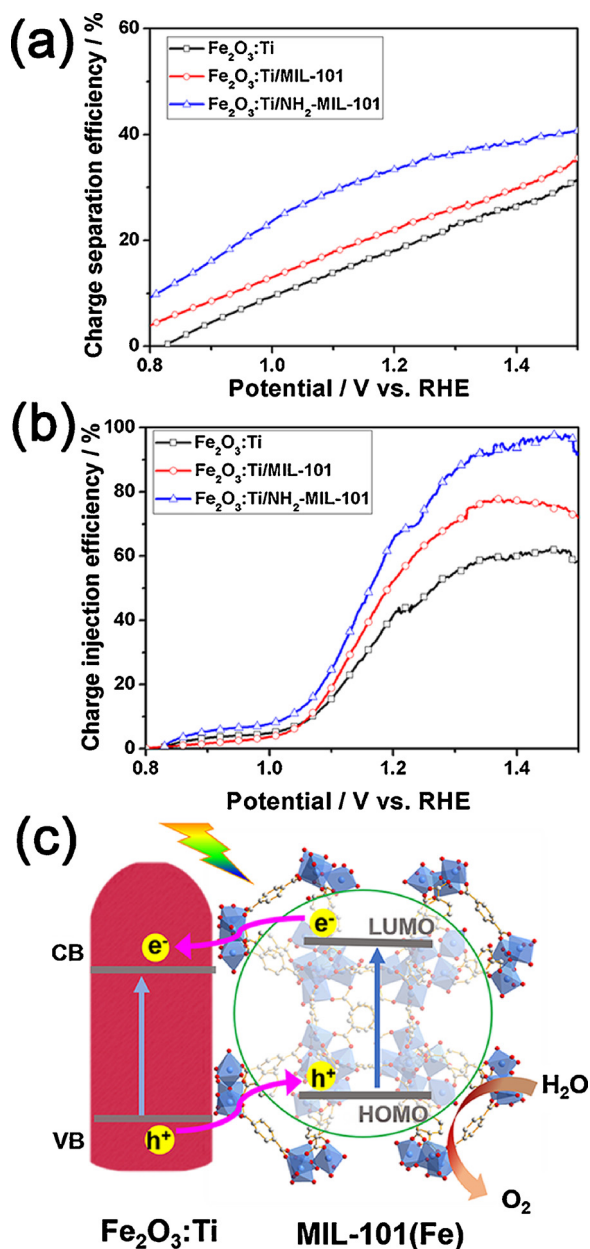
(a)

(b)

(c)

Fig. 6. (a) Charge separation efficiencies in the bulk and (b) charge injection efficiencies on the surface of different photoanodes; (c) Schematic presentation of band level positions for Fe_2O_3:Ti and MIL-101(Fe) showing the charge transfer path.

light harvesting efficiency and the charge separation as well as injection efficiency, the largely improved IPCE might be attributed to the enhanced light absorption as well as the accelerated charge transfer benefit from the Fe_2O_3:Ti/MOF heterostructure. The underlying reasons will be discussed in detail below.

In fact, the well-controlled MOF ultrathin film was crucial to the PEC response (Fig. S9). Although enhanced visible-light absorption was achieved for the sample fabricated in absence of PVP, this composite electrode showed positively shifted onset potential and similar photocurrent (0.97 mA cm^{-2}) to pristine Fe_2O_3: Ti electrode, which can be attributed to the poor connection between Fe_2O_3 nanorod and big MOF particles and the resulted poorer conductivity of thicker film. When uniform NH_2-MIL-101(Fe) coating began to form, the photocurrent density increased and reached the maximum value when the thickness of MOF shell reached ~5 nm (2.27 mA cm^{-2} for 2 PVP), then decreased slightly with increasing the thickness further (1.97 mA cm^{-2} for 5 PVP) though its light absorption capacity increased slightly. The possible reason was that the excess insulated PVP polymer molecules adsorbed on the surface of Fe_2O_3 nanorod may impair the charge transfer between Fe_2O_3 and MOF, and the thicker MOF film may also suffer from poor conductivity. These results further revealed that the critical step to acquire excellent semiconductor/MOFs composite material was constructing tight contact between them, and here the nanoscale MOF coating ensured the synergic action of two components to produce optimized efficacy.

In addition to catalytic activity, stability is another important factor to evaluate the performance of photoanode. As demonstrated in Fig. 5d, after "light on" state at 1.23 V *vs.* RHE for 2500 s, the corresponding photostability of the photoanode, expressed as the ratio of the residual photocurrent density to that of the initial value [35], was 88.9% and 86.7% for Fe_2O_3:Ti and Fe_2O_3:Ti/NH_2-MIL-101(Fe) photoanode, respectively. Besides, no obvious morphology and phase structure changes can be found in SEM and TEM images and XRD patterns of composite photoanode after the stability test (Figs. S10–S12), which indicated the excellent stability of the MOF-based core/shell nanocomposite during the PEC water oxidation process. We reckon this enhanced stability origins from the ultrathin MOFs film and the tight connection between MOFs and inorganic semiconductor.

3.5. Charge transfer behavior characterization

To shed more light on the function of the MOF shell on water oxidation kinetics of composite photoanodes, the charge separation efficiency (η_{sep}) and charge injection efficiency (η_{inj}) were examined *via* a hole-scavenger-assisted PEC measurement [36,37]. The η_{sep} and η_{inj} of both bare Fe_2O_3:Ti and Fe_2O_3:Ti/MOF composites were calculated according to the method reported previously [38], using the PEC response data measured with and without the addition of H_2O_2 as hole scavenger in the electrolyte (Fig. S13). As shown in Fig. 6a, the Fe_2O_3:Ti/MOF composite electrodes exhibit superior η_{sep} over the whole test range than the pristine Fe_2O_3:Ti electrode. Specifically, the η_{sep} of Fe_2O_3:Ti/MIL-101(Fe) and Fe_2O_3:Ti/NH_2-MIL-101(Fe) at 1.23 V *vs.* RHE was calculated to be 23.4% and 34.5%, about 1.2 and 1.8 folds than that of Fe_2O_3:Ti (19.4%). As the hematite photoanode suffers a lot from the poor conductivity and short hole diffusion length [39], the enhanced charge separation efficiency of the composite electrode should be attributed to the type II heterostructure formed by Fe_2O_3:Ti and Fe-based MOF. Fig. 6c illustrates the band level positions of Fe_2O_3:Ti and MIL-101(Fe) based upon the Tauc curves (Fig. S7) and the published data [26,34], which showed a typical staggered band structure. Upon light irradiation, the photo-generated electrons and holes are separated effectively by transferring electrons from the LUMO level of MIL-101(Fe) to the conduction band (CB) of Fe_2O_3:Ti and holes migrating inversely to accumulate on the HOMO level of MIL-101(Fe), which availably restrain the charge recombination [40], Interestingly, the amino functionalized MOF-based sample showed higher η_{sep} than the counterpart,

decreased in a trend similar to LSV curves: Fe_2O_3:Ti/NH_2-MIL-101(Fe) > Fe_2O_3:Ti/MIL-101(Fe) > Fe_2O_3:Ti. It is obvious that the Fe_2O_3:Ti/NH_2-MIL-101(Fe) core/shell photoanode exhibited the best PEC performance for water oxidation, which is comparable or even superior to most of the reported Fe_2O_3-based or MOF-based photoanodes (Table S1 and S2). To investigate the effect of MOF shell on the PEC performance, the external quantum efficiency of different photoanodes was evaluated by incident-photon-to-electron conversion efficiency (IPCE) measurement. Fig. 5c plots the spectral response of different photoanodes at an applied external potential of 1.23 V *vs.* RHE. Both the two Fe_2O_3:Ti/MOF photoanodes showed higher IPCE value than that of pristine Fe_2O_3:Ti over the whole range of 365–600 nm, which is in accordance with the enhanced absorption spectra. The value at 365 nm for Fe_2O_3:Ti/MIL-101(Fe) and Fe_2O_3:Ti/NH_2-MIL-101(Fe) was 28.2% and 42.3%, respectively, which was 1.5 and 2.3 folds of that of Fe_2O_3:Ti (18.8%). Given the fact that IPCE value is affected by the

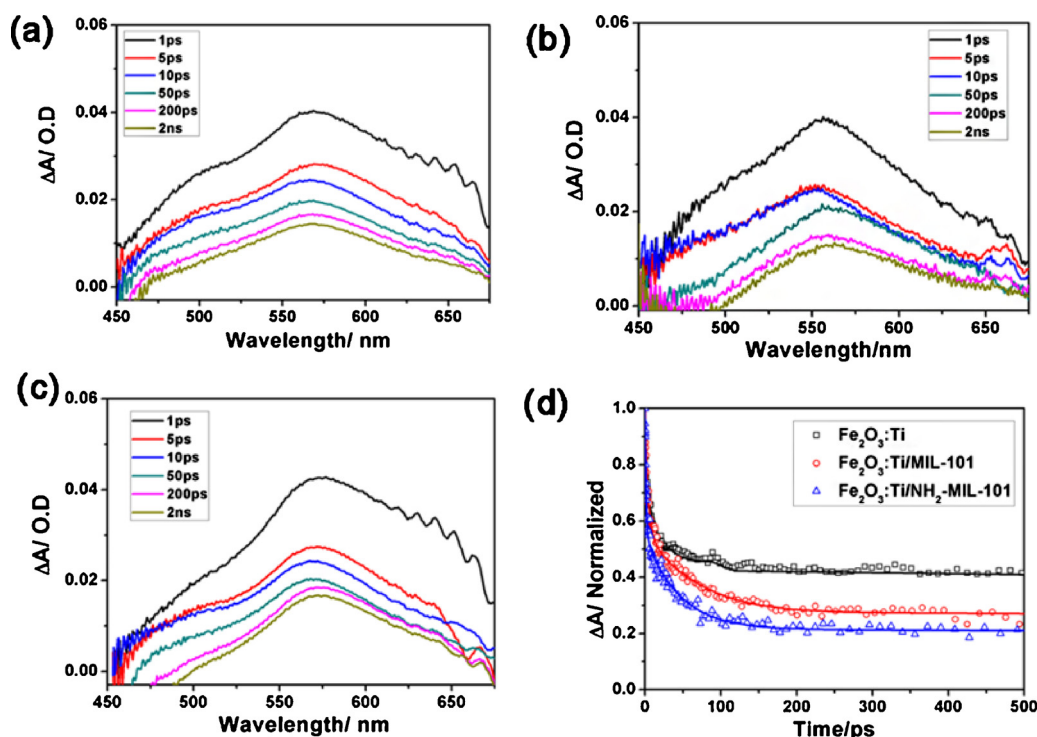**Fig. 7.** Optical transient absorption spectra recorded at different time delays, up to 2 ns: (a) Fe_2O_3:Ti; (b) Fe_2O_3:Ti/MIL-101(Fe) and (c) Fe_2O_3:Ti/NH_2-MIL-101(Fe); (d) Transient absorption decay curves at 570 nm of different photoanodes upon 355 nm (200 μJ cm^{-2}, 1000 Hz).
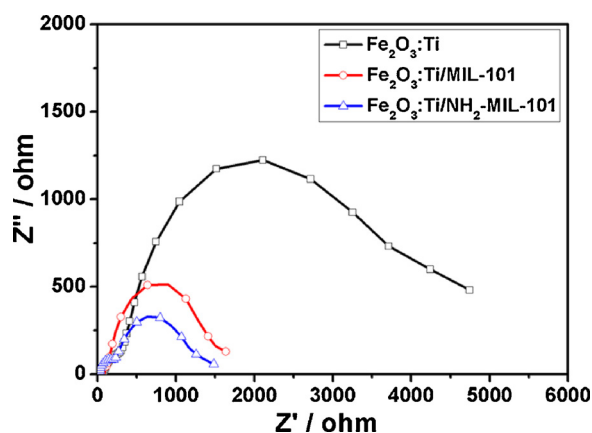

Fig. 8. PEIS plots of different photoanodes measured at 1.23 V *vs*. RHE under illumination of 100 mW cm^{-2}.

as the specific kinetic of amino group which can act as a hole stabilizer by delocalizing the hole from the exited Fe-O cluster toward the organic ligand and thus prolong the lifetime of the photo-excited state [41,42]. As far as the η_{inj} was concerned, similarly, Fe_2O_3:Ti/NH_2-MIL-101(Fe) photoanode manifested the highest value of 69.3% at 1.23 V *vs*. RHE, much higher than that of Fe_2O_3:Ti (44.7%) and Fe_2O_3:Ti/MIL-101 (59.3%) (Fig. 6b). Higher η_{inj} is the indicative of faster water oxidation rate. The enhanced η_{inj} of the MOF-modified electrode may be explained as the well dispersed Fe-O clusters within the ultrathin porous framework film served as quantum dots to shorten the migration length of the holes and provide more accessible active sites, thus lead to a faster water oxidation kinetics [27]. This is believed to be one of the significant advantage of MOF catalysts. On the other hand, the higher charge separation efficiency means more photo-generated holes survive from the migration process and accumulate on catalyst surface, resulting in a higher oxidation ability [43,44].

Furthermore, ultrafast transient absorption spectroscopy (TAS) was

performed to monitor the photoexcited carrier dynamics. Here the ultrafast dynamic behaviors in picoseconds-nanoseconds range were focused, as it was reported to be relevant to the charge transfer process [45]. When pumped at 355 nm, both pristine Fe_2O_3 and the composite samples showed a broadband positive absorption in the region 450–700 nm with a maximum absorption at ~570 nm (Fig. 7a–c), which was assigned to the signal of surface-trapped holes of Fe_2O_3 [46,47]. While the pure MOF did not show detectable signal under the same test condition [48]. The absorption decay curves of different electrodes at 570 nm were plotted in Fig. 7d and the fitting parameters were summarized in Table S3. All the samples showed fast decay in picosecond time scale while the decay rates for Fe_2O_3:Ti/MOF samples were much faster especially for Fe_2O_3:Ti/NH_2-MIL-101(Fe). The lifetime $\tau_{1/2}$ decreased from 31.6 ps of the Fe_2O_3:Ti to 17.8ps for Fe_2O_3:Ti/MIL-101(Fe) and 7.43 ps for Fe_2O_3:Ti/NH_2-MIL-101(Fe). The fast decay of the absorption signal implied that the MOF shell served as a hole-extraction layer to remove the surface-trapped holes from Fe_2O_3 nanorod to MOF on picosecond time scale. This process should benefit the charge separation as well as suppressing the electron/hole recombination. The charge transfer kinetics of composite photoanodes were scrutinized further by photoelectrochemical impedance spectroscopy (PEIS) measurements. As shown in Fig. 8, two semicircles can be found in Nyquist plots with the big semicircle at lower frequency related to the charge transfer resistance at photoanode/electrolyte interface, while the other smaller one corresponds to the charge carrier transport resistance inside the photoelectrode [49,50]. Clearly, the arch of Fe_2O_3:Ti/NH_2-MIL-101(Fe) was smaller than that of Fe_2O_3:Ti/MIL-101(Fe) and both of them were much smaller than that of Fe_2O_3:Ti, implying that modification of MOF shell significantly accelerate the hole injection into electrolyte to achieve higher reaction activity. This result is consistent with the observation from the PEC measurement, charge separation and injection efficiency described above. All the observations indicate that the Fe_2O_3:Ti/MOF heterostructure can work as a quite promising catalyst for photocatalytic water oxidation.

4. Conclusion

In this study, we propose a facile surfactant-assisted solvothermal method to fabricate Fe_2O_3:Ti/MOF core/shell composite electrodes which exhibit excellent PEC water oxidation performances. The morphology and thickness of MOF coating can by tuning the concentration of PVP surfactant, and uniform MOF films of several nanometers thick can be obtained. Detailed optical, photoelectrochemical and charge dynamical behavior investigation reveal that the ultrathin NH_2-MIL-101(Fe) shell can contribute a lot to the enhanced visible-light harvesting and facilitate the photo-generated charge separation through effective charge transfer with the core semiconductor; meanwhile, accelerates the hole injection efficiency that boosts the catalytic activity for oxygen evolution. Moreover, the amino group functionalized ligand is found to be beneficial to both the light absorption and the stabilization of the photoexcited state. Considering the diversity of photocatalytic MOFs, it is anticipated this research may pave an effective avenue to develop MOFs based catalysts for photocatalysis or photoelectrochemical application.

Acknowledgements

Appendix A. Supplementary data

Supplementary material related to this article can be found, in the online version, at doi: https://doi.org/10.1016/j.apcatb.2018.05.059.

References

[1] J. Ran, T.Y. Ma, G. Gao, X.-W. Du, S.Z. Qiao, Porous P-doped graphitic carbon nitride nanosheets for synergistically enhanced visible-light photocatalytic H_2 production, Energy Environ. Sci. 8 (2015) 3708–3717.

[2] M. Wen, K. Mori, Y. Kuwahara, T. An, H. Yamashita, Design and architecture of metal organic frameworks for visible light enhanced hydrogen production, Appl. Catal. B: Environ. 218 (2017) 555–569.

[3] L. Duan, L. Tong, Y. Xu, L. Sun, Visible light-driven water oxidation-from molecular catalysts to photoelectrochemical cells, Energy Environ. Sci. 4 (2011) 3296–3313.

[4] Z. Liang, C. Qu, W. Guo, R. Zou, Q. Xu, Pristine metal-organic frameworks and their composites for energy storage and conversion, Adv. Mater. (2017) 1702891.

[5] J. Qin, S. Wang, X. Wang, Visible-light reduction CO_2 with dodecahedral zeolitic imidazolate framework ZIF-67 as an efficient co-catalyst, Appl. Catal. B: Environ. 209 (2017) 476–482.

[6] J. Qiu, X. Zhang, Y. Feng, X. Zhang, H. Wang, J. Yao, Modified metal-organic frameworks as photocatalysts, Appl. Catal. B: Environ. 231 (2018) 317–342.

[7] G. Wang, Y. Liu, B. Huang, X. Qin, X. Zhang, Y. Dai, A novel metal-organic framework based on bismuth and trimesic acid: synthesis, structure and properties, Dalton Trans. 44 (2015) 16238–16241.

[8] L. Chi, Q. Xu, X. Liang, J. Wang, X. Su, Iron-based metal-organic frameworks as catalysts for visible light-driven water oxidation, Small 12 (2016) 1351–1358.

[9] C. Zhang, L. Ai, J. Jiang, Solvothermal synthesis of MIL–53(Fe) hybrid magnetic composites for photoelectrochemical water oxidation and organic pollutant photodegradation under visible light, J. Mater. Chem. A 3 (2015) 3074–3081.

[10] X.P. Chen, Z.X. Zhang, L.N. Chi, A.K. Nair, W.F. Shangguan, Z. Jiang, Recent advances in visible-light-driven photoelectrochemical water splitting: catalyst nanostructures and reaction systems, Nano-Micro Lett. 8 (2016) 1–12.

[11] T. Zhang, W. Lin, Metal-organic frameworks for artificial photosynthesis and photocatalysis, Chem. Soc. Rev. 43 (2014) 5982–5993.

[12] K. Shen, L. Zhang, X.D. Chen, L.M. Liu, D.L. Zhang, Y. Han, J.Y. Chen, J.L. Long, R. Luque, Y.W. Li, B. Chen, Ordered macro-microporous metalorganic framework single crystals, Science 359 (2018) 206–210.

[13] Y. Wang, M. Zhao, J. Ping, B. Chen, X. Cao, Y. Huang, C. Tan, Q. Ma, S. Wu, Y. Yu, Q. Lu, J. Chen, W. Zhao, Y. Ying, H. Zhang, Bioinspired design of ultrathin 2D bimetallic metal-organic-framework nanosheets used as biomimetic enzymes, Adv. Mater. 28 (2016) 4149–4155.

[14] K.G. Laurier, E. Fron, P. Atienzar, K. Kennes, H. Garcia, M. Van der Auweraer, D.E. De Vos, J. Hofkens, M.B. Roeffaers, Delayed electron-hole pair recombination in iron(III)-oxo metal-organic frameworks, Phys. Chem. Chem. Phys. 16 (2014) 5044–5047.

[15] P. Falcaro, R. Ricco, A. Yazdi, I. Imaz, S. Furukawa, D. Maspoch, R. Ameloot,

[16] J.D. Evans, C.J. Doonan, Application of metal and metal oxide nanoparticles@ MOFs, Coord. Chem. Rev. 307 (2016) 237–254.

[17] M. Zhao, K. Yuan, Y. Wang, G. Li, J. Guo, L. Gu, W. Hu, H. Zhao, Z. Tang, Metal-organic frameworks as selectivity regulators for hydrogenation reactions, Nature 539 (2016) 76–80.

[18] M. Wen, K. Mori, Y. Kuwahara, H. Yamashita, Plasmonic Au@Pd nanoparticles supported on a basic metal–organic framework: synergic boosting of H2 production from formic acid, ACS Energy Lett. 2 (2017) 1–7.

[19] J.-D. Xiao, Q.C. Shang, Y.J. Xiong, Q. Zhang, Y. Luo, S.-H. Yu, H.-L. Jiang, Boosting photocatalytic hydrogen production of a metal–organic framework decorated with platinum nanoparticles: the platinum location matters, Angew. Chem. Int. Ed. 55 (2016) 9389–9393.

[20] R. Li, J. Hu, M. Deng, H. Wang, X. Wang, Y. Hu, H.L. Jiang, J. Jiang, Q. Zhang, Y. Xie, Y. Xiong, Integration of an inorganic semiconductor with a metal-organic framework: a platform for enhanced gaseous photocatalytic reactions, Adv. Mater. 26 (2014) 4783–4788.

[20] G. Lu, J.T. Hupp, Metal-organic frameworks as sensors: a ZIF-8 based Fabry-Pe´rot device as a selective sensor for chemical vapors and gases, J. Am. Chem. Soc. 132 (2010) 7832–7833.

[21] V. Rubio-Giménez, S. Tatay, F. Volatron, F.J. Martínez-Casado, C. Martí-Gastaldo, E. Coronado, High-quality metal–organic framework ultrathin films for electronically active interfaces, J. Am. Chem. Soc. 138 (2016) 2576–2584.

[22] I. Hod, M.D. Sampson, P. Deria, C.P. Kubiak, O.K. Farha, J.T. Hupp, Fe-porphyrin-based metal-organic framework films as high-surface concentration, heterogeneous catalysts for electrochemical reduction of CO_2, ACS Catal. 5 (2015) 6302–6309.

[23] M.-S. Yao, W.-X. Tang, G.-E. Wang, B. Nath, G. Xu, MOF thin film-coated metal oxide nanowire array: significantly improved chemiresistor sensor performance, Adv. Mater. 28 (2016) 5229–5234.

[24] W.W. Zhan, Q. Kuang, J.Z. Zhou, X.J. Kong, Z.X. Xie, L.S. Zheng, Semiconductor@ metal-organic framework core-shell heterostructures: a case of ZnO@ZIF-8 nanorods with selective photoelectrochemical response, J. Am. Chem. Soc. 135 (2013) 1926–1933.

[25] G. Huang, D.M. Yin, L.M. Wang, A general strategy for coating metal–organic frameworks on diverse components and architectures, J. Mater. Chem. A 4 (2016) 15106–15116.

[26] D. Wang, R. Huang, W. Liu, D. Sun, Z. Li, Fe-based mOFs for photocatalytic cO_2 reduction: role of coordination unsaturated sites and dual excitation pathways, ACS Catal. 4 (2014) 4254–4260.

[27] Y. Horiuchi, T. Toyao, K. Miyahara, L. Zakary, D.D. Van, Y. Kamata, T.H. Kim, S.W. Lee, M. Matsuoka, Visible-light-driven photocatalytic water oxidation catalysed by iron-based metal-organic frameworks, Chem. Commun. 52 (2016) 5190–5193.

[28] Y.-F. Xu, X.-D. Wang, H.-Y. Chen, D.-B. Kuang, C.-Y. Su, Toward high performance photoelectrochemical water oxidation: combined effects of ultrafine cobalt iron oxide nanoparticle, Adv. Funct. Mater. 26 (2016) 4414–4421.

[29] J. Su, J. Wang, C. Liu, B. Feng, Y. Chen, L. Guo, On the role of metal atom doping in hematite for improved photoelectrochemical properties: a comparison study, RSC Adv. 6 (2016) 101745–101751.

[30] H. Sun, J. He, J. Wang, S.Y. Zhang, C. Liu, T. Sritharan, S. Mhaisalkar, M.Y. Han, D. Wang, H. Chen, Investigating the multiple roles of polyvinylpyrrolidone for a general methodology of oxide encapsulation, J. Am. Chem. Soc. 135 (2013) 9099–9110.

[31] G. Lu, S. Li, Z. Guo, O.K. Farha, B.G. Hauser, X. Qi, Y. Wang, X. Wang, S. Han, X. Liu, J.S. DuChene, H. Zhang, Q. Zhang, X. Chen, J. Ma, S.C. Loo, W.D. Wei, Y. Yang, J.T. Hupp, F. Huo, Imparting functionality to a metal-organic framework material by controlled nanoparticle encapsulation, Nat. Chem. 4 (2012) 310–316.

[32] H. Liu, J. Zhang, D. Ao, Construction of heterostructured $ZnIn_2S_4$@NH_2-MIL-125(Ti) nanocomposites for visible-light-driven H_2 production, Appl. Catal. B: Environ. 221 (2018) 433–442.

[33] S. Liu, L. Zheng, P. Yu, S. Han, X. Fang, Novel composites of α-Fe_2O_3 tetrakaidecahedron and graphene oxide as an effective photoelectrode with enhanced photocurrent performances, Adv. Funct. Mater. 26 (2016) 3331–3339.

[34] Y.-F. Xu, H.-S. Rao, B.-X. Chen, Y. Lin, H.-Y. Chen, D.-B. Kuang, C.-Y. Su, Achieving highly efficient photoelectrochemical water oxidation with a $TiCl_4$ treated 3D antimony-doped SnO_2 macropore/branched α-Fe_2O_3 nanorod heterojunction photoanode, Adv. Sci. 2 (2015) 150049.

[35] U. Shaislamov, K. Krishnamoorthy, S.J. Kim, W. Chun, H.-J. Lee, Facile fabrication and photoelectrochemical properties of a CuO nanorod photocathode with a ZnO nanobranch protective layer, RSC Adv. 6 (2016) 103049–103056.

[36] H. Dotan, K. Sivula, M. Grätzel, A. Rothschild, S.C. Warren, Probing the photoelectrochemical properties of hematite (α-Fe_2O_3) electrodes using hydrogen peroxide as a hole scavenger, Energy Environ. Sci. 4 (2011) 958–964.

[37] A.G. Tamirat, W.-N. Su, A.A. Dubale, H.-M. Chen, B.-J. Hwang, Photoelectrochemical water splitting at low applied potential using a NiOOH coated codoped (Sn, Zr) α-Fe_2O_3 photoanode, J. Mater. Chem. A 3 (2015) 5949–5961.

[38] Gurudayal, P.M. Chee, P.P. Boix, H. Ge, F. Yanan, J. Barber, L.H. Wong, Core-shell hematite nanorods: a simple method to improve the charge transfer in the photoanode for photoelectrochemical water splitting, ACS Appl. Mater. Interfaces 7 (2015) 6852–6859.

[39] P. Peerakiatkhajohn, J.H. Yun, H. Chen, M. Lyu, T. Butburee, L. Wang, Stable hematite nanosheet photoanodes for enhanced photoelectrochemical water splitting, Adv. Mater. 28 (2016) 6405.

[40] R. Marschall, Semiconductor composites: strategies for enhancing charge carrier separation to improve photocatalytic activity, Adv. Funct. Mater. 24 (2014) 2421–2440.

[41] J.G. Santaclara, M.A. Nasalevich, S. Castellanos, W.H. Evers, F.C. Spoor, K. Rock,

L.D. Siebbeles, F. Kapteijn, F. Grozema, A. Houtepen, J. Gascon, J. Hunger, M.A. van der Veen, Organic linker defines the excited-State decay of photocatalytic MIL-125(Ti)-type materials, ChemSusChem 9 (2016) 388–395.

[42] A. Walsh, C.R. Catlow, Photostimulated reduction processes in a titania hybrid metal-organic framework, ChemPhysChem 11 (2010) 2341–2344.

[43] J.-S. Yang, W.-H. Lin, C.-Y. Lin, B.-S. Wang, J.-J. Wu, n-Fe$_2$O$_3$ to N$^+$-TiO$_2$ heterojunction photoanode for photoelectrochemical water oxidation, ACS Appl. Mater. Interfaces 7 (2015) 13314–13321.

[44] J.Y. Kim, D.H. Youn, J.H. Kim, H.G. Kim, J.S. Lee, Nanostructure-preserved hematite thin film for efficient solar water splitting, ACS Appl. Mater. Interfaces 7 (2015) 14123–14129.

[45] K. Appavoo, M. Liu, C.T. Black, M.Y. Sfeir, Quantifying bulk and surface recombination processes in nanostructured water splitting photocatalysts via in situ ultrafast spectroscopy, Nano Lett. 15 (2015) 1076–1082.

[46] C.X. Kronawitter, L. Vayssieres, S. Shen, L. Guo, D.A. Wheeler, J.Z. Zhang,

B.R. Antoun, S.S. Mao, A perspective on solar-driven water splitting with all-oxide hetero-nanostructures, Energy Environ. Sci. 4 (2011) 3889.

[47] D.A. Wheeler, G. Wang, Y. Ling, Y. Li, J.Z. Zhang, Nanostructured hematite: synthesis, characterization, charge carrier dynamics, and photoelectrochemical properties, Energy Environ. Sci. 5 (2012) 6682–6702.

[48] L. Hanna, P. Kucheryavy, C. Liu, X. Zhang, J.V. Lockard, Long-lived photoinduced charge separation in a trinuclear iron-μ$_3$-oxo-based metal–organic framework, J. Phys. Chem. C 121 (2017) 13570–13576.

[49] M. Shao, F. Ning, M. Wei, D.G. Evans, X. Duan, Hierarchical nanowire arrays based on ZnO core−layered double hydroxide shell for largely enhanced photoelectrochemical water splitting, Adv. Funct. Mater. 24 (2014) 580–586.

[50] J. Hou, C. Yang, H. Cheng, S. Jiao, O. Takeda, H. Zhu, High-performance p-Cu$_2$O/n-TaON heterojunction nanorod photoanodes passivated with an ultrathin carbon sheath for photoelectrochemical water splitting, Energy Environ. Sci. 7 (2014) 3758–3768.